atmosphere

MDPI

Article

A Laboratory Model of the Large-Scale Atmospheric Circulation of Tidally Locked Exoplanets

Bálint Vass [1], Ádám Kadlecsik [1] and Miklós Vincze [2,3,*,†]

[1] Von Kármán Laboratory of Environmental Flows, Institute of Physics and Astronomy, Eötvös Loránd University, H-1117 Budapest, Hungary; vassbalint2003@gmail.com (B.V.); adam.kadlecsik@gmail.com (Á.K.)
[2] Department of Materials Physics, Eötvös Loránd University, H-1117 Budapest, Hungary
[3] HUN-REN Institute of Earth Physics and Space Science, H-9400 Sopron, Hungary
* Correspondence: mvincze@general.elte.hu
† Current address: Department of Theoretical Physics, ELKH-ELTE Theoretical Physics Research Group, Eötvös Loránd University, Pázmány P. stny. 1/A, H-1117 Budapest, Hungary.

Abstract: We report on a novel fluid dynamics experiment configuration based on a modified version of the differentially heated rotating annulus, a widely used laboratory model of the large-scale mid-latitude atmospheric circulation. Through applying an azimuthally (zonally) inhomogeneous, dipole-like thermal boundary condition—imitating a permanent "day side" and "night side" in the rotating setting—we explore the character of the flow patterns emerging at different values of the zonal temperature contrast and rotation rate. This configuration may prove to be a useful minimal model of the large-scale atmospheric circulation of tidally locked exoplanets.

Keywords: exoplanetary atmospheres; geophysical fluid dynamics; baroclinic instability; rotating annulus

Citation: Vass, B.; Kadlecsik, Á.; Vincze, M. A Laboratory Model of the Large-Scale Atmospheric Circulation of Tidally Locked Exoplanets. *Atmosphere* **2024**, *15*, 982. https://doi.org/10.3390/atmos15080982

Academic Editor: Leonardo Primavera

Received: 2 July 2024
Revised: 6 August 2024
Accepted: 13 August 2024
Published: 16 August 2024

1. Introduction

The large-scale circulation in the atmospheres of planetary bodies is primarily driven by the horizontal gradient of the incident solar heat flux falling on the surface. The resulting meridional temperature contrast maintains poleward material and momentum transport from the warmer equatorial regions [1]. On slowly rotating planets, such as Venus, these thermal boundary conditions lead to the emergence of single-cell meridional convection on each hemisphere. Faster spinning bodies, e.g., Earth, Mars, or Saturn's largest moon, Titan, exhibit more complex forms of atmospheric circulation that are characterized by a larger number of overturning cells with alternating dominant meridional flow directions [2].

The Rossby number Ro of such systems can be estimated as $Ro \sim U/(2\Omega L)$, where U is the typical flow (wind) velocity and L denotes the relevant horizontal length scale, e.g., the radius of the planet. Ro quantifies the relative contribution of the Coriolis force to the flow and is proportional to the ratio of the rotation period $T = 2\pi/\Omega$ (i.e., the duration of a sidereal or "intertial" day) and the hydrodynamic timescale $\tau \sim L/U$. For $Ro \gg 1$—as in the case of the planet Venus with $T \approx 243$ Earth days—the Coriolis effect is practically negligible, whereas in the $Ro \ll 1$ limit, it is dominant, yielding quasi-geostrophic flow. The order-of-magnitude estimates of Ro for the aforementioned planetary bodies are as follows: $Ro^{\text{Venus}} \sim 370$, $Ro^{\text{Mars}} \sim 0.2$, $Ro^{\text{Titan}} \sim 18$, and $Ro^{\text{Earth}} \sim 0.06$ [3].

A third timescale of relevance may be defined by the solar day (synodic rotation period) $T_\odot$ of the given planet, i.e., the duration between two subsequent sunrises. In the cases of Mars or Earth—except for the polar regions in summer and winter—the sidereal day and solar day are practically the same ($T \approx T_\odot$). On these bodies, the solar day is also much shorter than the hydrodynamic timescale ($T_\odot \ll \tau$); hence, the diurnal temperature variations average out and do not affect the general character of the large-scale atmospheric circulation. In the case of Venus, however, which has a solar day of 117 Earth days, the situation is just the opposite ($T_\odot \gg \tau$), and the atmospheric dynamics are largely

influenced by the slowly changing day–night thermal contrast. Moreover, the resulting thermal tide and the huge difference between its period and that of the sidereal day are found to be responsible for the so-called Eliassen–Palm momentum flux, which fuels the famous super-rotation of the Venusian upper atmosphere [4].

Due to the obvious observation bias—as short-period phenomena are easier to observe in a limited measurement time frame than slowly changing ones—the vast majority of the over 5000 extrasolar planets (exoplanets for short) discovered and confirmed to date [5] orbit very close to their host star, making their attitude necessarily tidally locked [6]. Therefore, their orbital period ("year") matches the duration of the sidereal day T. These periods—typically ranging from a few days to a few weeks—are presumably short enough to yield small Rossby numbers, Ro, at which the Coriolis force has a profound effect on the planet's atmospheric circulation. As a consequence of the tidal locking, the same hemisphere is always illuminated, rendering $T_\odot \to \infty$. The existence of permanent day and night sides poses a unique thermal boundary condition: the flow may then be primarily driven by the zonal—and not the meridional—temperature gradient.

Although the Earth- and space-based telescopes of the present day are not yet capable of direct observations of the atmospheric circulation patterns on exoplanets, there already exists a rapidly increasing pool of works investigating conceptual numerical models of the flow states in such systems [7]. Based on the data provided by instruments, such as the Kepler, TESS, and James Webb space observatories, it is possible to estimate the sidereal periods, the diameters, and—via spectroscopy—the compositions of exoplanet atmospheres [8]. Moreover, the characteristic wind speeds U of certain exoplanets have also been deduced from the observed Doppler shift and broadening of atmospheric spectral lines [9]. With such empirical data on U, Ω, and the length scale (planet radius) L, the Rossby number Ro of the large-scale atmospheric circulation of an exoplanet can be estimated.

Once the relevant nondimensional parameters of the system can be determined, as well as the basic geometry of the setting and its boundary conditions, one may attempt to construct a minimalistic experimental model based on the principle of hydrodynamic similarity. Our objective was to create such an apparatus to explore the combined effect of the permanent zonal thermal contrast and rotation. For this purpose, we modified the differentially heated rotating annulus, a classic apparatus to study the basic large-scale dynamics of a mid-latitude atmosphere.

The traditional configuration (sketched in the left panel of Figure 1) consists of a rotating annular gap whose inner sidewall is cooled and the outer one is heated; thus, the working fluid experiences a radial temperature gradient. These "traditional" thermal boundary conditions imitate the meridional differential incoming solar heat flux on the planet, and the key non-dimensional parameters can be set in the experiment to match those of actual planets.

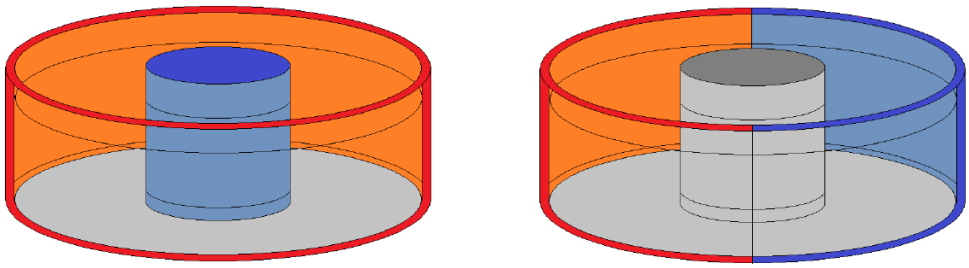

Figure 1. A schematic layout of the thermal boundary conditions of the differentially heated rotating annulus experiment in the traditional configuration (**left**) and in the "tidally locked exoplanet" configuration (**right**). Blue indicates cooling and the warm colors (red and orange) represent heating at the boundaries.

These parameters are the aforementioned Rossby number Ro, and the Taylor number Ta, which quantifies the importance of inertial forces relative to viscous forces [1]. Such

laboratory settings have been widely used for over half a century since the pioneering works of David Fultz, Raymond Hide, and their respective groups [10]; more recently, annulus experiments have proven to be useful test beds for the validation and benchmarking of numerical methods operational in weather forecasting [11,12], and they have contributed to the better understanding of temperature distribution transitions in our changing climate [13–15].

Our modified configuration is sketched in the right panel of Figure 1. In this version, the co-rotating heating and cooling boundary segments are both situated along the outer ("equatorial") sidewall—indicated here with the same colors as in the left panel, i.e., red for heating and blue for cooling—yielding a "dipole-like" reflectional antisymmetry in the forcing, which represents the thermal contrast between the day and night sides. We explored the general character of the temperature field in this configuration, the emerging characteristic temperature difference in the flow at various values of Ro, the typical "wind" speeds in the system, and the propagation patterns of passive tracers.

This paper is organized as follows. In Section 2, we describe our setup in detail and provide an overview of the applied data acquisition and evaluation methods. We present our results in Section 3 and then discuss the broader implications of our findings in Section 4.

2. Setup and Methods

The layout of the experiment platform is shown in the photo of Figure 2a. The rotating tank, mounted on a turntable, was separated into sections by 2 mm-thick co-axial cylindrical sidewalls made of copper. The working fluid (water) was placed into the annular gap between the inner cylinder (with a radius a = 4.5 cm) and the outer rim (with a radius b = 14.75 cm) (rendering the gapwidth as a characteristic length scale $L = b - a = 10.25$ cm). The water level was set to $H = 14.5$ cm in all performed experiment runs.

The baroclinic annulus of the von Kármán Laboratory (Eötvös University, Budapest) was modified for our measurements with the installation of electric heating elements—which are controlled by a thermostat—covering one half of the outer rim (as sketched in Figure 1a) and cooling elements that are mounted on the opposite side (Figure 2). The heating element consists of a fabric of heating wire wrapped around one side of the outer copper cylinder. The heating wire was attached to a co-rotating USB power source mounted on the rotating platform, and it was heated up to a maximum temperature of 75 °C (releasing a power of 2.5 W). This configuration is shown in red at the right hand side of the schematic of Figure 2c. Cooling was facilitated by two removable commercially available plastic ice packs (shown in blue in Figure 2), which were also placed onto the rotating platform so that they touched the copper sidewall at the opposing side. These cooling elements were filled with a mixture of water and propylene glycol and were initially cooled down to −17.5 °C in a laboratory freezer. The geometrical dimensions of the two ice packs were 22 cm × 15 cm × 2 cm. The bottom plate of the cylindrical rotating tank was made of a ca. 2 cm thick acrylic disk.

After setting the temperature boundary conditions and initiating rotation at the required angular velocity Ω (ranging from 0.47 rad/s to 2.59 rad/s), we waited at least 30 min for the flow to develop before starting the data acquisition. We evaluated 16 experiment runs in total, corresponding to different settings of Ro, and processed 58 infrared images and 5 video recordings of the developed flow.

The tank was left uncovered to facilitate the observation of water surface temperature fields and the sidewall temperatures using a thermal camera. A VarioCAM® HR Inspect (680/30 mm) infrared imager (manufactured by InfraTec GmbH in Dresden, Germany) was mounted above the tank onto a co-rotating tripod facing downward, as shown in Figure 2. The field of view—as seen in the non-rotating control image in Figure 2b—of the acquired 640 pixel × 480 pixel thermograms covered the entire free water surface and the vertical outer rim in its vicinity with a thermal resolution of 0.01 °C (note that, due to perspective

distortion of the camera looking into the tank from above, the vertical sidewalls were also captured above the water level).

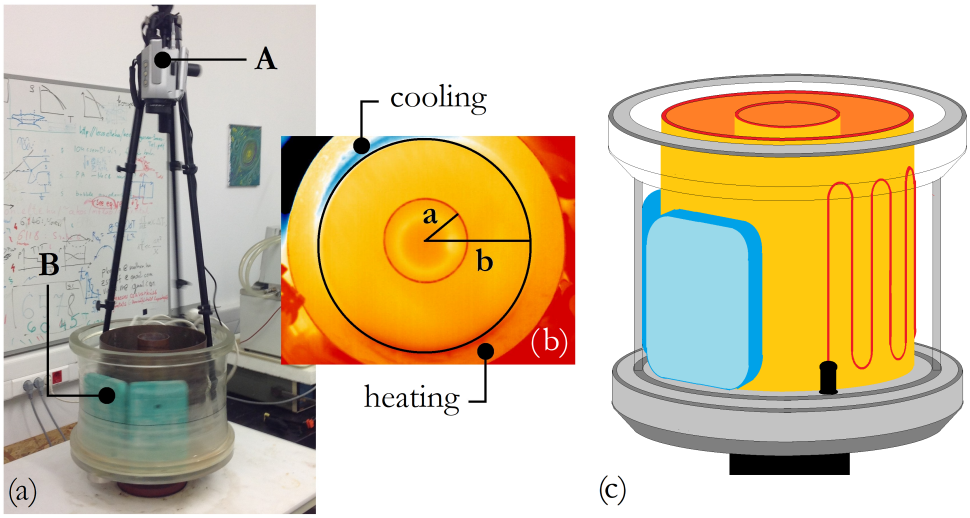

Figure 2. The experimental setup.MV:Done (**a**) The rotating annulus of the von Kármán Laboratory mounted on the turntable with the co-rotating infrared imager (marked with A) and the cooling elements (marked with B). (**b**) Infrared test image from a non-rotating baseline run. The radii of the inner and outer cylinders—$a = 4.5$ cm and $b = 14.75$ cm, respectively—are indicated. (**c**) Schematics of the experiment setup showing the placement of the heating wire (red) and the ice packs (blue).

The acquired infrared images were pre-processed using VarioCAM® IRBIS® 3 thermography software (created by InfraTec GmbH in Dresden, Germany). Then, one-dimensional temperature profiles as a function of the azimuthal angle ϕ were extracted from each thermogram: one from the part that shows the "forcing temperature" $T_f(\phi)$ at the outer sidewall just above the water surface along a circular contour of radius $r = b$ from the center (e.g., along the violet circle shown in Figure 3a yielding the blue curve in Panel b); and the azimuthal profile $\overline{T}(\phi)$ of the surface temperature field averaged over the gapwidth over the radial distances $a < r < b$ (as shown in a black curve in Figure 3b).

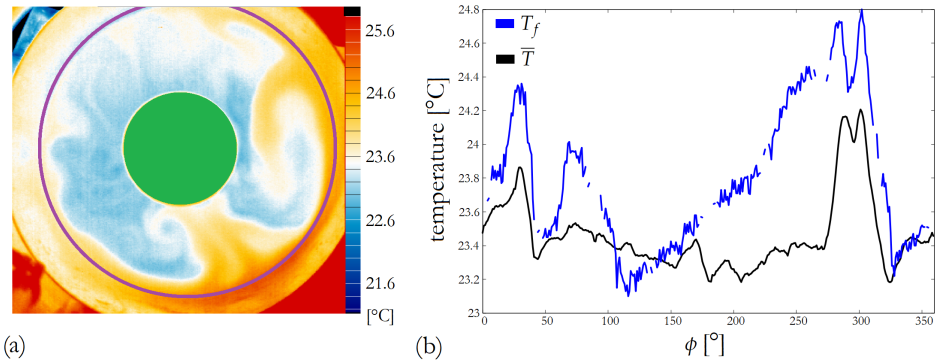

Figure 3. Demonstration of the data processing. (**a**) An infrared image of the water surface and the vertical sidewall taken from above. The forcing surface temperature profile $T_f(\phi)$ was extracted along the violet contour, whereas the radially averaged water surface temperature profiles were evaluated in the annular domain between the inner cylinder (masked with a green circle here) and the violet circle. (**b**) The resulting temperature profiles $T_f(\phi)$ (blue) and $\overline{T}(\phi)$ were acquired from the image of Panel (**a**).

In a few runs, a co-rotating camera operating in the visual range (the CCD camera of an Apple iPad 2 tablet, manufactured by Foxconn Inc. in Shenzhen, China) was also installed onto the same tripod, capturing 1920 pixel × 1080 pixel frames of the water surface

in time-lapse mode, i.e., at a 2 fps temporal resolution. In these experiments, blue food dye was injected manually from a syringe into the water, and the spreading of this passive tracer cloud in the flow was evaluated from the video recordings using the Tracker 6.0.9 video analysis tool [16].

3. Results

3.1. Qualitative Description of the Flow

Four selected typical water-surface temperature fields are shown in Figure 4 from different runs. The Rossby number values given under each panel were derived from the assumption that approximate thermal wind balance holds in the system; thus, the characteristic velocity scale U in the buoyancy-driven flow can be estimated as

$$U = \frac{\alpha g H \Delta T_f}{2\Omega L}, \tag{1}$$

where $\alpha = 2.1 \cdot 10^{-4}$ 1/K is the volumetric thermal expansion coefficient of the water at room temperature, g is the acceleration of gravity, and ΔT_f is the temperature contrast driving the flow [17].

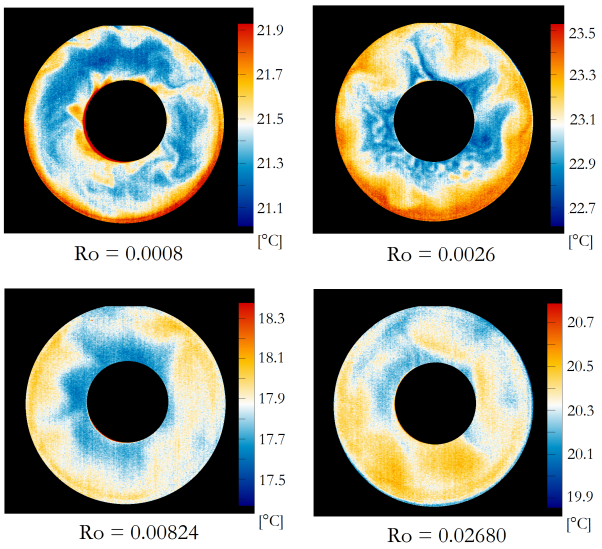

Figure 4. Infrared images of the thermal water surface patterns from four typical experiments (the thermal Rossby numbers *Ro* are indicated). The parts of the images showing the inner cylinder and the outer parts of the setup are masked with red. The heating element is to the bottom and the cooling is to the top in each panel.

Then, the definition $Ro = U/(2\Omega L)$ yields

$$Ro = \frac{\alpha g H \Delta T_f}{4\Omega^2 L^2}, \tag{2}$$

which is a form referred to as the thermal Rossby, or Hide, number [10]. For the calculations we took, ΔT_f appeared to be the difference between the maximum and minimum temperatures measured in the $T_f(\phi)$ forcing profile.

In the $Ro = 0.0026$ case of Figure 4, it is clearly visible that the surface temperature field was rather similar to those observed in the quasigeostrophic *Ro* regime of the traditional configuration, showing irregular Rossby wave-like patterns [18]. However, this form appeared to inherit the "left-right" symmetry of the thermal boundary conditions; we note that these images were aligned such that the coldest point of the outer rim was to the top and the warmest was to the bottom. This also implies—as confirmed by our observations—that, although the pattern may change in shape over time, it does not move

in the zonal direction, which is in contrast with the "eastward" propagating Rossby waves of the traditional rotating annulus setting with axially symmetric boundary conditions [19]. This, however, does not mean that the flow is not in quasigeostrophic balance: passive tracers tend to follow the isotherms, as will be demonstrated later in Section 3.3. In this case, the flow at the cooled side was characterized by alternating warm and cold plumes between the rim and the inner cylinder—which was warmer than the cooled side but colder than the heated sidewall.

In the other three cases shown in Figure 4, no clear symmetry can be noticed. At $Ro = 0.0008$, the character of the temperature field is similar to that of the $Ro = 0.0026$ case in the sense that, at the heated side, the warm, few centimeter-wide boundary layer appears more pronounced than at the cooled side. In this run, again, eddies appeared at the cooled side in the vicinity of the wall but their diameter was smaller than the large plumes at $Ro = 0.0026$. This is in agreement with the expected scaling: the Rossby radius of deformation L_d is inversely proportional to the rotation rate Ω [1]. Thus, if the temperature contrast ΔT is approximately constant, it scales with $\sqrt{Ro}$.

In the two bottom panels of Figure 4, which represent higher Rossby numbers ($Ro = 0.00824$ and $Ro = 0.0268$), no such eddies are visible. The character of the flow in this regime more resembles the transition between the axially symmetrical state to the Rossby wave state in the traditional configuration, which happens around $Ro \sim 1$, but, in the "exoplanet" configuration, this already occurs at much lower thermal Rossby numbers.

3.2. Temperature Fluctuations and the Anisotropy of the Flow

Next, we compared the temperature contrast parameter ΔT_f of the forcing in each experiment with the temperature difference observed between the highest and lowest values of the "meridionally averaged" $\overline{T}(\phi)$ temperature profiles of the water surface (hereafter marked as $\Delta\overline{T}_{\max}$). The acquired scatter plot is shown in Figure 5a. The dotted diagonal line marks the $y = x$ equality. Apparently, in all but one measurement, $\Delta\overline{T}_{\max} < \Delta T_f$ held, i.e., the temperature anomalies at the water surface were generally below the forcing temperature contrast, as was expected.

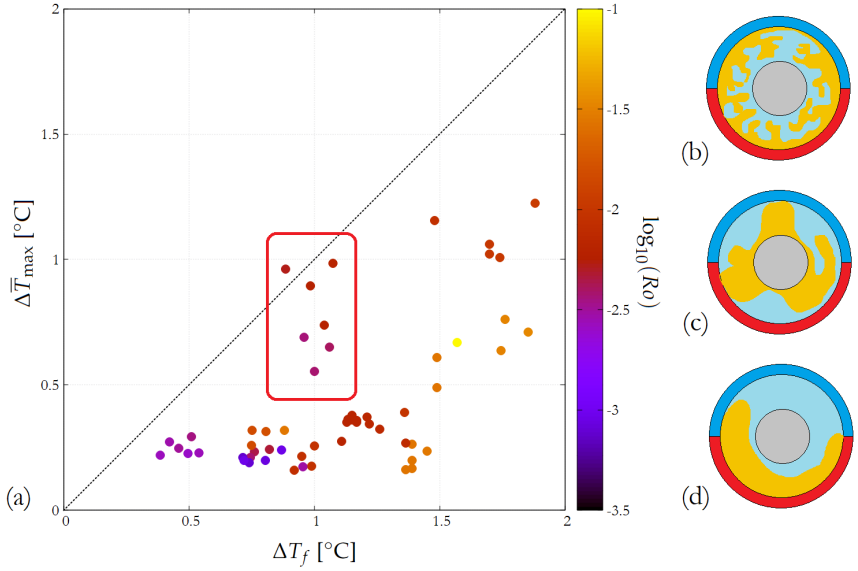

Figure 5. Different states of the flow in terms of surface temperature fluctuations. (**a**) Scatter plot of the observed temperature range $\Delta\overline{T}_{\max}$ of the radially averaged zonal temperature profiles as a function of the forcing temperature contrast ΔT_f. (**b**–**d**) Sketches of the different flow patterns showing the $L_d \ll L$; $L_d \approx L$; and $L_d > L$ cases.

It has to be emphasized that, however, the calculation of $\Delta\overline{T}_{\max}$ involves averaging over the radial ("meridional") direction. This procedure implies that if the temperature

field was axially symmetrical in the statistical sense—meaning that there were no significant azimuthal variations between the radial means—then we would always find $\Delta\overline{T}_{\max} \approx 0$, even in the presence of marked radial temperature differences. Therefore, this parameter—besides being, in part, determined by the scale of temperature fluctuations—is also a measure of azimuthal ("zonal") anisotropy.

Three somewhat distinct clusters—or branches—of the data points can be identified in Figure 5a. First, there was a horizontal branch scattering around $\Delta\overline{T}_{\max} \approx 0.25$ °C, mainly in the region $\Delta T_f \lesssim 1$ °C. The coloring of the points followed $\log_{10}(Ro)$, and the fact that a wide range of Ro-values appeared on this branch implies that the constant nature of this branch is not directly related to rotation rate Ω. Instead, it seems to indicate a threshold phenomenon in ΔT_f; unless the forcing temperature contrast reaches a certain critical value, the thermally driven flow on larger scales was blocked by, e.g., viscous damping regardless of Ω. This was also the case in the traditional setting of the rotating annulus: below a certain (radial) ΔT_f, only axially symmetrical modes can develop even if $Ro \ll 1$ holds [19].

This axial symmetry, however, is understood in a statistical sense here and does not mean that small-scale eddies are not present in this flow state. An example for such a case is shown in Figure 4 (the panel for $Ro = 0.0008$ corresponding to $\Delta T_f = 0.805$ °C), where several coherent structures can be identified. Yet, these were irregularly distributed and had typical length (correlation) scales that were much smaller than the length scale of the setup, gapwidth L, thus keeping $\Delta\overline{T}_{\max}$ small; this property is sketched in Figure 5b.

At $\Delta T_f \approx 1$ °C, the large-scale circulation was not blocked by viscosity any more, and—from there—on the values of $\Delta\overline{T}_{\max}$, an increasing trend was clearly shown. However, around this value, a roughly vertical branch also appeared, and it is marked by a red rectangle in Figure 5. The seven data points all corresponded to runs in the $0.0039 \lesssim Ro \lesssim 0.0063$ Rossby number range. This is an indication of a state in which the characteristic size of the irregular surface temperature anomalies approach the horizontal scale L, as sketched in Figure 5c. Here, the irregularly shaped warm eddies can already be organized in such a configuration that they stretch through the whole gapwidth at certain values of ϕ, yielding larger than average $\overline{T}(\phi)$ values, and, thus, a larger $\Delta\overline{T}_{\max}$ parameter. However, these fluctuations do not necessarily align in such a way; hence, the large vertical spread of these data points in the plot.

The data points of the $\Delta T_f > 1.25$ °C range showed an increasing trend, and all corresponded to larger Rossby numbers, implying larger deformation radii than the characteristic scale of the setting $L_d > L$. Here, there was less irregularity in the surface temperature (see, e.g., the thermogram and temperature profiles of Figure 3, corresponding to a $\Delta T_f \approx 1.3$ °C run) and the warm plumes crossed the entire gap. Therefore, the value of $\Delta\overline{T}_{\max}$ in this regime was determined more by the modulus of the forcing temperature contrast ΔT_f than the spatial configuration of the temperature anomalies.

3.3. Tracer Spreading in the Flow

In five additional experiments, we investigated the propagation dynamics of passive tracer clouds in the flow. Our objective was to evaluate whether the formula of Equation (1)—based on the assumption of thermal wind balance—provides an appropriate estimate of the actual observable flow speeds in the studied configuration. In the injected water drops, blue food food dye was dissolved, which is a tracer material that practically has the same density as the working fluid.

Two sequences of snapshots captured by a co-rotating camera were taken at thermal Rossby numbers $Ro = 0.00092$ for (a) and $Ro = 0.028$ for (b). The corresponding rotation rates were $\Omega = 2.34$ rad/s for (a) and $\Omega = 0.47$ rad/s for (b); hence, these covered 67 and 20 revolutions of the rotating tank, respectively. The color balance and contrast of the images were adjusted for better visibility. It should be noted that, as this device—unlike the infrared imager—was not placed precisely above the axis of rotation, a part of the free water surface was blocked in the field of view by the inner cylinder of the tank. This artifact was masked in the images, yielding the oddly shaped white areas in which we

displayed the elapsed time from the first snapshot. The dye patterns can also be compared to those in the infrared images that—marked with "IR" in Figure 6—were captured at the end of the each sequence. One may notice that the dye patterns tended to spread along the boundary of the colder (blue colored) domain, indicating that the assumption that the flow is quasi-geostrophic appears to be well established.

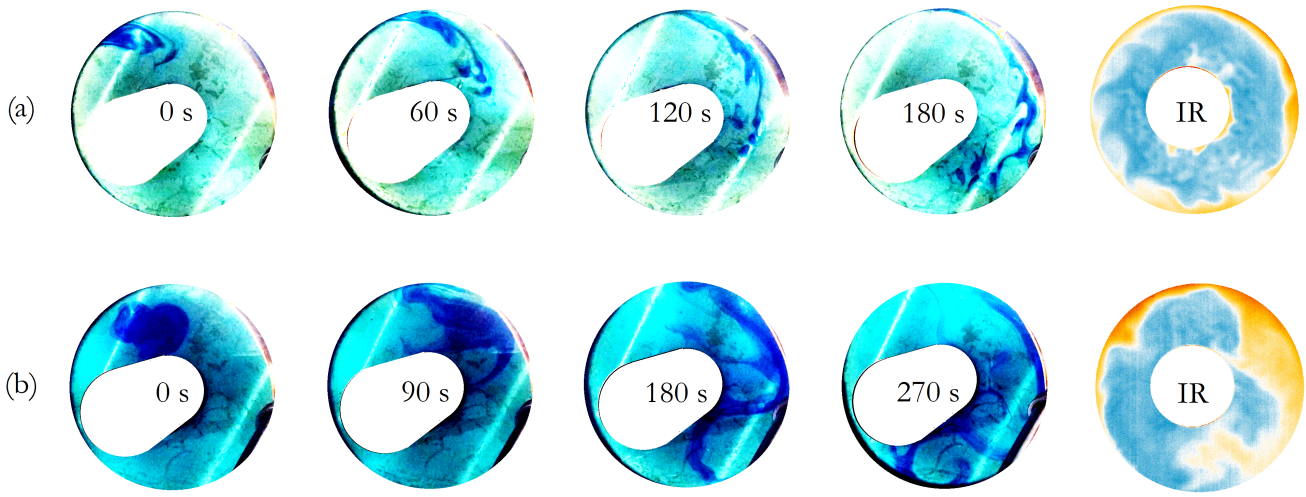

Figure 6. Sequences of snapshots showing tracer propagation and the corresponding infrared (IR) surface temperature pattern. The elapsed time is marked at the center of each image. (**a**) The internally heated control experiment with a thermal Rossby number (calculated—inadequately—from the sidewall heating temperature contrast only) of $Ro = 0.00092$. (**b**) An experiment with normal (tidally locked exoplanet) forcing conditions, where $Ro = 0.028$.

It is worth mentioning that, in all runs, the propagation was *retrograde*, i.e., its prevailing direction relative to the rotating tank was the opposite ("westward") to that of the tank with respect to the laboratory frame. In the case of Sequence a), it is clearly a consequence of the special boundary condition applied for this particular case. In this single measurement, the temperature of the inner cylinder wall—otherwise not regulated in our experiments—was set to be markedly higher than the average water-surface temperature. The radial temperature contrast between the cylinder wall and the fluid was measured to be $\delta T \approx 1.2$ °C, whereas this difference in typical runs—as the one in Sequence b) of Figure 6—was found to be an order of magnitude smaller at $\delta T \approx 0.1$ °C. Moreover, in this special run, δT was also larger than the zonal temperature forcing contrast itself, i.e., $\Delta T_f = 0.72$ °C. Thus, the clockwise ("westward") flow in this case was clearly the consequence of the thermal wind that develops in the unusual setting of boundary conditions, which are reversed compared to the traditional rotating annulus configuration (where the inner cylinder is cooled, initiating a "poleward" momentum flux that deviates eastward by the Coriolis effect). Here, the opposite sign of the meridional temperature gradient yielded an opposite flow direction. Nevertheless, it is worth emphasizing that the flow direction was also retrograde in Series (b), where no significant heating occurred at the inner cylinder; thus, the flow was clearly driven by the zonal forcing $\Delta T_f = 0.88$ °C.

Next, the propagation of selected parts of the tracer cloud was tracked in the recorded videos using the Tracker 6.0.9 video analysis tool, and, from a linear regression of the zonal displacement time series $r(t)\phi(t)$, the slope of the fitted lines was taken as the estimate of the average zonal speed u_ϕ. As different parts of the initial cloud propagated at different rates, this procedure yielded a range of u_ϕ values, whose averages are given as the data points of Figure 7 as a function of the theoretical prediction with Equation (1), which is based on the measured zonal temperature contrast T_f. The length of the error bars corresponded to the maximum difference between the observed drift rates in each given run.

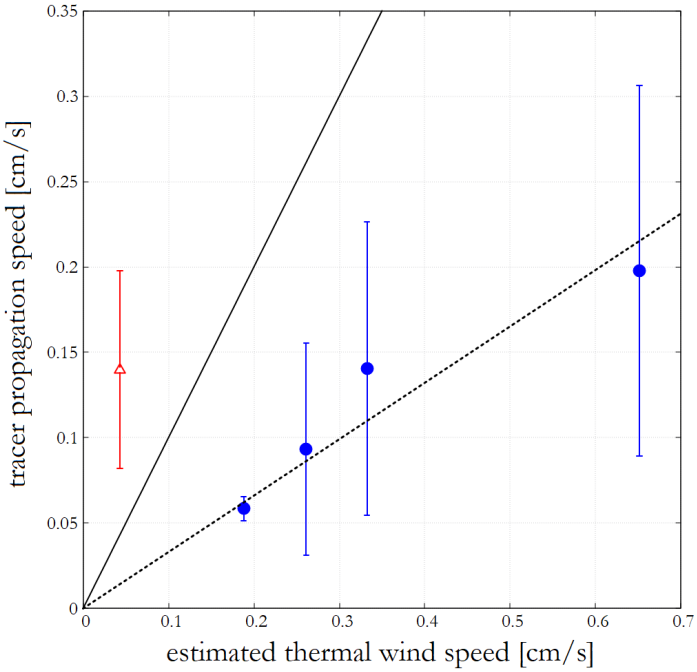

Figure 7. Contrasting the thermal wind balance-based estimates of the flow speed and the measured tracer propagation speeds. The blue data points mark the "normal" experiments, and the red triangle denotes the internally heated reference run, as shown in Figure 6a. The solid line represents $y = x$, and the dotted line is the $y = 0.33x$ fit to the (blue) data points.

The red triangular data point corresponds to the aforementioned special case, where the flow was not driven by ΔT_f but by the radial contrast; therefore, it was not surprising that the formula underestimated the drift rates.

The solid black line in the plot represents the $y = x$ line of perfect agreement between the estimated and measured drift speeds. Clearly, all of the other four data points from the "normal" experiments (blue circles) scattered under this line and appeared to roughly follow a trend line of $y = 0.33(\pm 0.03)x$ (where the range given in the parenthesis is the least square error of the fit to the data points), indicating that the thermal wind balance appears to hold if considered with an empirical correction factor of around $1/3$.

4. Discussion

In this pilot study, we performed laboratory experiments in a modified version of the differentially heated rotating annulus experiment, which—to the best of our knowledge—has never been conducted. Such experiments can be useful for exploring the large-scale atmospheric flows of given *particular* exoplanets once their relevant parameters of hydrodynamic similarity—e.g., the Rossby number *Ro*—can be determined from observations.

Although the direct imaging of the weather in exoplanetary atmospheres seems to be out of reach with the astronomical instruments of the present and the near future, there already exist some promising results in determining the characteristic wind speeds of certain exoplanets from the shape and position of their spectral lines [9]. The authors expect an explosive increase in such data in the foreseeable future now that the James Webb Space Telescope, launched in late 2021, is fully operational and can provide infrared spectra of exoplanetary atmospheres at an unprecedented clarity [20].

In the present study, we intentionally focused on the Rossby number *Ro* as this is the only relevant parameter combination that is expected to become accessible for a larger number of tidally locked exoplanets relatively soon (since planet diameter, rotation rate, and characteristic wind speeds are the only reasonably available quantities). It is to be noted, however, that—just as in the case of the traditional rotating annulus setting—other nondimensional parameters related to kinetic energy dissipation and measures of the ef-

fects of "eddy viscosity" and "eddy diffusivity", e.g., Taylor, Rayleigh, or Ekman numbers, also affect the flows in rotating planetary atmospheres. Deducing these parameters—from spectral data only—seems to be rather challenging. From the measured atmospheric composition and relying on "educated guesses" based on known analogs—such as planetary bodies in our solar system—it may also become possible to address the viscosity-related aspects of these atmospheric circulations. It should be noted, however, that, in the present study, we did not intend to model an actual confirmed exoplanet but to explore the character of the flow in a wide range of *Ro* in this thus-far-untried configuration as a preparation for targeted investigations in the future.

Regarding the scalability of the results from laboratory experiments to actual planets, it is important to emphasize that the Rossby number *Ro* can be considered the relevant (nondimensional) scale parameter in planetary atmospheres as long as the Coriolis effect plays a dominant role in the circulation. This practically implies that, in the $Ro \ll 1$ regime, the circulation patterns in a differentially heated rotating annulus setting are expected to resemble the ones of a real planet in a qualitative sense, as has been widely demonstrated for the case of Earth's mid-latitude atmosphere throughout the rich history of rotating annulus experiments since the 1950s. However, for the $Ro \sim 1$ range (and above), other processes become more relevant, rendering the laboratory results less adequate. Also, it is only in the small-*Ro* regime that the assumption of thermal wind balance, which requires quasi-geostrophy for estimating wind speeds—as in Equation (1)—is valid.

Furthermore, our minimalistic model is built on the approximation that the zonal (day–night) temperature contrast is the key boundary condition driving the circulation. However, this assumption does not necessarily hold for all exoplanets. Either varying surface albedos or a Venus-like dense atmosphere with a strong greenhouse effect can result in such conditions where the thermally driven circulation is driven primarily by, e.g., vertical or meridional temperature gradients instead, yielding very different flow states.

Another clear limitation of such experiments in general is that they are unable to capture the dynamics arising from the curvature of the spherical planetary body, which is first and foremost the so-called β-effect [1], i.e., the latitude-dependence of the Coriolis force. It is well understood, for instance, that, in fast rotating planets, the ($Ro \ll 1$) β-effect leads to the formation of zonal regions of alternating wind directions, as in the case of, e.g., the Hadley or Farrel cells of Earth or the spectacular stripes of Jupiter [3]. In the absence of the β-effect—as in the "flat" experiment—such patterns cannot develop; hence, the flow in the experiment instead represents the dynamics of a zonal domain (a meridional overturning cell with thermal wind) of the atmosphere and whose actual width is set by the so-called Rhines scale [1] of a real planet.

After mentioning these limitations, the question may arise in the reader of what data in this experimental setup (and the presented results) can contribute to a better understanding of real atmospheres that cannot be obtained via numerical simulations just as effectively. Indeed, a substantial pool of numerical analyses already exist in the atmospheric circulation of tidally locked exoplanets from general circulation models of varying complexity [7]. However, since it is not possible to observe such systems at a resolution that facilitates the direct detection of atmospheric patterns, these numerical results cannot be tested and validated. Note that, in our solar system, there is no planet that is tidally locked to the Sun that could possible used as a test case. Laboratory experiments, on the other hand, can serve as test beds, and—despite the simplified geometry and boundary conditions—can provide certain benchmark settings with which the findings from simulations can be contrasted. Comparisons of this kind between the classic rotating annulus setting and numerical model results (in terms of, e.g., drift rates, and the general character of Rossby waves) have proven to be useful in the validation and fine tuning of terrestrial atmospheric circulation models; hence, they have already contributed to making weather forecasts more accurate [11].

5. Conclusions

The main findings of our experiment campaign are as follows. We observed that, despite the thermal boundary conditions being largely different from those driving the mid-latitude atmospheric circulation of Earth-like planets, the emerging flow may still exhibit Rossby wave-like patterns even if their zonal propagation is practically inhibited by the permanent day–night temperature contrast. We were able to distinguish between the different flow regimes in terms of their zonal symmetry properties (anisotropy) as a function of the forcing temperature contrast ΔT_f and Rossby number Ro. We demonstrated that tracer propagation in such systems appears to be dominantly retrograde (as a consequence of the interplay between zonal temperature contrast and the Coriolis force) and generally seems to scale with the formula derived from the assumption of a thermal wind balance with an empirical correction factor of 1/3.

Follow-up experiments are in preparation to explore the combined effect of meridional and zonal temperature contrasts and to survey the flow regimes as a function of the "zonal-" and "meridional thermal Rossby numbers" that are defined accordingly. Another planned extension of these preliminary experiments will address the effects of a thermal tide-like forcing [21], i.e., such a zonal temperature contrast that is not stationary with respect to the co-rotating reference frame but moves around at a period $T_\odot$ different from the sidereal day T. Such experiments may contribute to a better understanding of the super-rotation phenomenon that is known to exist in the upper atmosphere of Venus [4] and is also hypothesized to develop in the atmospheres of exoplanets [22].

Author Contributions: Conceptualization, M.V.; methodology, B.V. and M.V.; software, B.V. and Á.K.; validation, B.V., Á.K. and M.V.; running the experiments, B.V. and M.V.; resources, M.V.; writing—original draft preparation, M.V. All authors have read and agreed to the published version of the manuscript.

Funding: Á.K. was supported by the ÚNKP-23-2 New National Excellence Program of the Ministry for Innovation and Technology from the source of the National Research, Development and Innovation Fund.

Data Availability Statement: Measured raw data are available upon request from the corresponding author (M. Vincze) due to software-specific non standard file formats.

Acknowledgments: The authors are grateful for the fruitful discussions with T. Tél, M. Herein, D. Jánosi, and Z. Trócsányi. M.V. wishes to thank A. Kohári, B. Vincze, and the Maicsirke research group for their personal support. The helpful assistance and flexibility of Managing Editor Adriana Ouyang is also highly appreciated.

Conflicts of Interest: The authors declare no conflicts of interest. The funders had no role in the design of this study; in the collection, analyses, or interpretation of data; in the writing of the manuscript; or in the decision to publish the results.

References

1. Vallis, G. *Atmospheric and Oceanic Fluid Dynamics*, 2nd ed.; Cambridge University Press: Cambridge, UK, 2017.
2. Wang, Y.; Read, P.L.; Tabataba-Vakili, F.; Young, R.M.B. Comparative terrestrial atmospheric circulation regimes in simplified global circulation models. Part I: From cyclostrophic super-rotation to geostrophic turbulence. *Q. J. R. Meteorol. Soc.* **2018**, *144*, 2537–2557. [CrossRef]
3. Read, P.L. Dynamics and circulation regimes of terrestrial planets. *Planet. Space Sci.* **2011**, *59*, 900–914. [CrossRef]
4. Horinouchi, T.; Hayashi, Y.-Y.; Watanabe, S.; Yamada, M.; Yamasaki, A.; Kouyama, T.; Taguchi, M.; Fukuhara, T.; Takagi, M.; Ogohara, K.; et al. How waves and turbulence maintain the super-rotation of Venus' atmosphere. *Science* **2020**, *368*, 405–409. [CrossRef] [PubMed]
5. Lee, C.H. Exoplanets: Past, present, and future. *Galaxies* **2018**, *6*, 51. [CrossRef]
6. Wang, Y.; Mora, P.; Liang, Y. A direct numerical verification of tidal locking mechanism using the discrete element method. *Celest. Mech. Dyn. Astron.* **2022**, *134*, 42. [CrossRef]
7. Heng, K.; Showman, A.P. Atmospheric dynamics of hot exoplanets. *Annu. Rev. Earth Planet. Sci.* **2015**, *43*, 509–540. [CrossRef]
8. Burrows, A.S. Spectra as windows into exoplanet atmospheres. *Proc. Natl. Acad. Sci. USA* **2014**, *111*, 12601–12609. [CrossRef] [PubMed]

9. Seidel, J.V.; Ehrenreich, D.; Pino, L.; Bourrier, V.; Lavie, B.; Allart, R.; Wyttenbach, A.; Lovis, C. Wind of change: Retrieving exoplanet atmospheric winds from high-resolution spectroscopy. *Astron. Astrophys.* **2020**, *633*, A86. [CrossRef]
10. Ghil, M.; Read, P.; Smith, L. Geophysical flows as dynamical systems: The influence of Hide's experiments. *Astron. Geophys.* **2010**, *51*, 4–28. [CrossRef]
11. Vincze, M.; Borchert, S.; Achatz, U.; von Larcher, T.; Baumann, M.; Hertel, C.; Remmler, S.; Beck, T.; Alexandrov, K.; Egbers, C. Benchmarking in a rotating annulus: A comparative experimental and numerical study of baroclinic wave dynamics. *Meteorol. Z.* **2015**, *23*, 611–635. [CrossRef]
12. Young, R.M.B.; Read, P.L. Data assimilation in the laboratory using a rotating annulus experiment. *Q. J. R. Meteorol. Soc.* **2013**, *139*, 1488–1504. [CrossRef]
13. Harlander, U.; Borcia, I.D.; Vincze, M.; Rodda, C. Probability distribution of extreme events in a baroclinic wave laboratory experiment. *Fluids* **2022**, *7*, 274. [CrossRef]
14. Harlander, U.; Sukhanovskii, A.; Abide, S.; Borcia, I.D.; Popova, E.; Rodda, C.; Vasiliev, A.; Vincze, M. New laboratory experiments to study the large-scale circulation and climate dynamics. *Atmosphere* **2023**, *14*, 836. [CrossRef]
15. Vincze, M.; Hancock, C.; Harlander, U.; Rodda, C.; Speer, K. Extreme temperature fluctuations in laboratory models of the mid-latitude atmospheric circulation. *Sci. Rep.* **2023**, *13*, 20904. [CrossRef] [PubMed]
16. Tracker Video Analysis and Modeling Tool. Available online: https://physlets.org/tracker/ (accessed on 2 July 2024).
17. Vincze, M.; Jánosi, I.M. Laboratory experiments on large-scale geophysical flows. In *The Fluid Dynamics of Climate*; Provenzale, A., Ed.; Springer: Heidelberg, Germany, 2016; pp. 61–94.
18. Vincze, M.; Harlander, U.; von Larcher, T.; Egbers, C. An experimental study of regime transitions in a differentially heated baroclinic annulus with flat and sloping bottom topographies. *Nonlinear Process. Geophys.* **2014**, *21*, 237–250. [CrossRef]
19. Harlander, U.; Kurgansky, M.V.; Speer, K.; Vincze, M. Baroclinic instability from an experimental perspective. *C. R. Phys.* 2024, *accepted*.
20. Constantinou, S.; Madhusudhan, N.; Gandhi, S. Early insights for atmospheric retrievals of exoplanets using JWST transit spectroscopy. *Astrophys. J. Lett.* **2023**, *943*, L10. [CrossRef]
21. Auclair-Desrotour, P.; Laskar, J.; Mathis, S. Atmospheric tides in Earth-like planets. *Astron. Astrophys* **2017**, *603*, A107. [CrossRef]
22. Showman, A.P.; Polvani, L.M. Equatorial superrotation on tidally locked exoplanets. *Astrophys. J.* **2011**, *738*, 71. [CrossRef]